DEGREE PROJECT

Improving the experimental setup for ultrasound -optical tomography imaging

Ibtisam Ahmed

Engineering Physics and Electrical Engineering, master's level
2023

Luleå University of Technology
Department of Engineering Science and Mathematics

LULEÅ
UNIVERSITY
OF TECHNOLOGY

[This page intentionally left blank]

Improving the experimental setup for ultrasound-optical tomography imaging

Author: Ibtisam Ahmed

Supervisor : Dr. Akvile Zabiliute-Karaliune
Examiner : Professor Kerstin Ramser

Engineering Physics and Electrical Engineering
master's level

Department of Engineering Sciences and Mathematics
Luleå University of Technology, Sweden
June 16, 2023

Abstract

According to *Bröstcancer förbundet*, mammography is not efficient at detecting tumors in dense breast tissue or diagnosing breast cancer at its early stages. Ultrasound-optical tomography (UOT) is an imaging technique in development and has the potential for deep-tissue imaging. If ultrasound-optical tomography were implemented, it would be easier to differentiate between malignant, benign, and healthy tissue from any type of breast tissue.

UOT is an imaging technique that takes advantage of high penetration depth and high spatial resolution of ultrasound imaging and optical imaging. In UOT, a laser light and an ultrasound pulse propagate through the tissue simultaneously at a frequency f_L and f_{US}, respectively. The light will scatter while it propagates through the tissue and some of this scattered light will become frequency shifted by ultrasound pulse due to the acousto-optic effect. The tagged light will have the frequency $f_T = f_L + f_{US}$. The tagged (frequency shifted) light can be separated from the untagged light (unshifted light) using a thulium-doped lithium niobate, Tm^{3+}: $LiNbO_3$, crystal as a filter. The crystal is kept at a temperature close to zero kelvin because then it exhibits unique characteristics, e.g. it has a narrow linewidth and long-lived hyperfine levels at this temperature. The filter is created by a method known as spectral hole burning (SHB). A laser beam is used to transfer electrons from the ground state to the excited state to create a hole at a specific wavelength. The spectral hole is created at the frequency of the tagged light and hence a narrow bandpass filter is constructed inside the crystal. The tagged light is fully transmitted through the filter while it highly attenuates untagged light. The tagged light is detected with a photodiode and processed in MATLAB after it has been transferred to an oscilloscope.

This thesis aims to model and design a phantom probe that minimizes vibration and other unwanted movements or disturbances during measurements. The automated phantom holder will be used for the recording of 3D images. Another task of the thesis was to obtain the absorption spectrum of a 0.005% Tm^{3+}: $LiNbO_3$ crystal when it is cooled down to 3 K to ensure that the crystal has the same absorption characteristics as predicted in literature. The absorption line at $\sim$ 800 nm is of interest since oxyhemoglobin and deoxyhemoglobin have similar absorption coefficients at $\sim$ 800 nm. Optical absorption and scattering information will help determine if the sample contains a cancerous region.

The phantom probe was modeled in Solid Works and manufactured through 3D printing. In this setup, the sample holder was chosen to be translated while the ultrasound transducer was stationary to generate less blurry images. The design of the probe has to accommodate two detection schemes, reflection and transmission mode. The phantom probe was automated using a linear servo actuator since it was controlled with pulse-width modulation (PWM). It used a square signal as an input that could be generated with an Arbitrary signal generator (AWG). Using a device that operates with a signal was important because it would make it easier to integrate it into the experimental

setup. The whole phantom probe was constructed in a cost-efficient way and in a way that it could be easily incorporated into the experimental setup.
The absorption spectrum showed that the crystal has an absorption line at $\sim$ 794.3 nm. This absorption spectrum was compared to an absorption spectrum taken at 8 K on the same crystal and captured with a different method. Both absorption spectra had the same absorption peaks at almost the same wavelengths but they also showed few discrepancies that may depend on the temperature difference and the recording method. In this thesis, the absorption spectrum data taken was captured by sweeping the wavelength. The signal was captured with a photodiode, transferred to an oscilloscope, and then processed in MATLAB. The absorption spectrum data at 8 K was obtained using a Fourier transform spectrometer, resulting in data with little noise and well resolved peaks.

To conclude, a functional and robust phantom probe was designed and manufactured that could withstand vibration and other undesired movements. An absorption spectrum of Tm^{3+}: $LiNbO_3$ crystal was obtained at 3 K and compared to absorption taken at 8 K and compared to literature and previous measurements under similar conditions.

List of abbreviations

AOM Acousto-optical modulator

AWG Arbitrary waveform generator

CNR Contrast-to-noise ratio

CW Continuous wave

HbO_2 Oxyhemoglobin

Hb Deoxyhemoglobin

PMT photo-multiplier tube

RE Rare-earth-ions

SHF Spectral-hole filtering

SNR Signal-to-noise ratio

Tm^{3+}:$LiNbO_3$ Thulium lithium niobate

UOT Utrasound-optical tomography

UST Utrasound transducer

Contents

1 Introduction

This section will contain a short presentation of the most common imaging techniques in the medical field and gives an introduction to ultrasound-optical tomography.

1.1 Background

According to *Bröstcancer Förbundet* around 7 570 Swedish women were diagnosed with breast cancer in 2020. Around 40% of all women in Sweden were estimated to have very dense breast tissue and they were five to six times more likely to have cancer compared to women with less compact tissue [1].

Mammography is the main detection method for breast cancer screening and it uses X-rays to take an image[2]. Mammography is not suited for diagnosing and determining if a lump is malignant or benign. Mammography is not sensitive enough for soft tissue to distinguish between benign or malignant tumors, which is a huge drawback. The current diagnostics methods lack decent resolution and contrast for imaging soft tissue. It is also difficult to perform deep-tissue imaging with the currently available methods. X-ray imaging, computer-aided tomography (CAT) scans, and magnetic resonance imaging (MRI) are a few imaging tools that are diligently used in healthcare. The drawback of these techniques is that they are ionized, sensitive to external disturbance, and expensive. They operate with limited imaging depth and lack sufficient contrast to avoid biopsy [3, 4]. It becomes problematic when imaging breasts that mainly consist of fat and can be of any length. There is a need to differentiate between cancerous and healthy soft tissue and determine if the tumor is malignant.

Diffuse optical tomography (DOT) is another near-infrared imaging technique and its contrast can be compared to ultrasound optical tomography. DOT is a technique that has been around longer than UOT but it has only resolution in the order of millimeters compared to UOT's micrometer resolution [5]. There is also optical coherence tomography (OCT), an imaging technique that can reach a very good spatial resolution of a few micrometers but it lacks the imaging depth that is possible with UOT[6, 7]. A technique almost similar to UOT is Photo-acoustic tomography (PAT). This imaging technique combines optical imaging with ultrasound imaging and has been around longer than UOT. In PAT, pulses of light propagate through the tissue and the ultrasound signal measures the thermoelastic expansion of the tissue[8].

Ultrasound(-modulated) optical tomography, also known as Acousto-optical tomography (AOT), is a technique that can perform deep tissue imaging by combining ultrasound with optical imaging. The first experimental demonstration of UOT occurred in 1993 [9]. In UOT, a laser beam illuminates a small part of the tissue while an ultrasound (US) pulse propagates through the tissue. The light scatters immediately as it hits the surface of the tissue, while an ultrasound pulse propagates ballistically through the tissue[10]. By combining these techniques, the advantages of these techniques get highlighted. Acoustic waves from an ultrasound pulse are used to penetrate deep into the tissue, while visible and near-infrared light is used for good resolution. A UOT

image with good contrast is obtained when a few photons that have penetrated deep into the tissue get entangled with the acoustic waves. The laser light will become frequency-shifted when it propagates through the ultrasound field and become tagged with the ultrasound frequency. The detected light will consist of untagged photons with the frequency f_L and tagged photons with a frequency of $f_T = f_L + f_{US}$. The background signal will be larger compared to the signal used for imaging. This demands a filter that highly attenuates untagged light. A Tm^{3+}:$LiNbO_3$ crystal is therefore used to discriminate between tagged and untagged photons. According to literature [11], Tm^{3+}: $LiNbO_3$ has an absorption line at $\sim$ 794.22 nm since it is where the absorption coefficient of oxyhemoglobin and deoxyhemoglobin overlap, as shown in Figure 1.

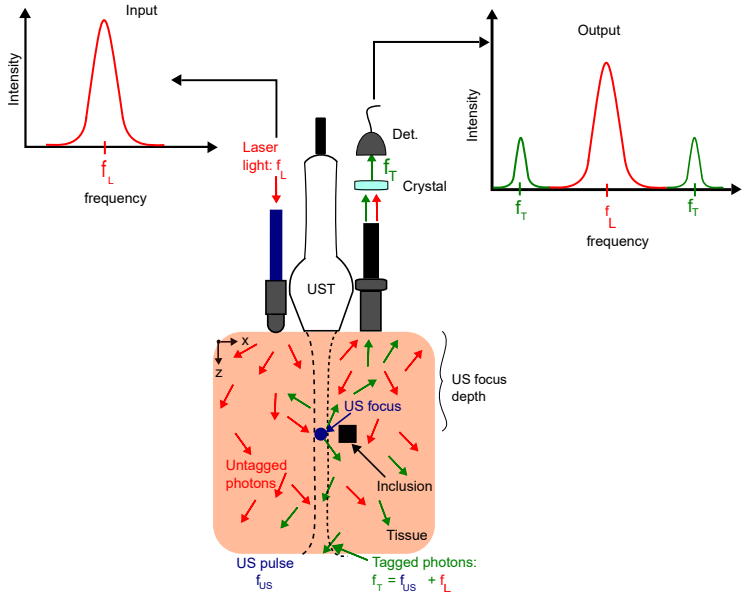

Figure 1: Principle of UOT explained through reflection geometry. Photons with a frequency of f_L enter the tissue and scatter in random directions (red arrow). The US pulse (dashed lines) creates a focus (the blue circle) with the frequency f_{US}. A fraction of the laser photons traverse the ultrasound (US) pulse (green arrow) and become frequency shifted by multiples of the ultrasound frequency f_{US}. The tagged photons (green arrow) will have the frequency $f_{tot} = f_L + f_{US}$. The tagged and untagged light is collected by the light guide (right of UST) and tagged light is filtered out with a crystal. Detection of the shifted photons enables spatially resolved optical contrast measurements inside the tissue. Adapted from [9].

PAT can only obtain the optical absorption properties of tissue, and on the other hand, UOT can obtain absorption-, scattering-, and mechanical properties in one measurement. PAT reaches less imaging depth compared to UOT, further, when using UOTcontrast-to-noise (CNR) improves as the imaging depth increases when using UOT [10]. The comparison is summarized in table 1. One of the main challenges for UOT is overcom-

Table 1: Comparing ultrasound optical tomography (UOT) with optical coherence tomography (OCT) and photo-acoustic tomography (PAT [12]

Properties	**OCT**	**DOT**	**UOT/PAT**
Contrast	Good	Excellent	Excellent (= DOT)
Resolution	Excellent ($\sim$ 10 μm)	Poor ($\sim$ 5 mm)	Exellent
Imaging depth	Poor	Excellent	Good and scalable
Speckle artifacts	Strong	None	None
Scattering	Strong	Strong	–
Coefficient	($\sim$ 100/cm)	($\sim$ 100/cm)	–

ing the difficulty of detecting low signals in the presence of a high background signal (typically $\sim$ six orders of magnitude). It is also challenging to perform in vivo imaging because it is difficult to overcome the decorrelation time (< 1 ms) of biological tissue; to maintain coherence, i.e. the signals must be captured below that time [13].
Despite the advantages of UOT, there are some drawbacks. It requires a rare-earth-ion doped crystal which is very expensive and takes time to produce. It also needs a cryostat to cool the crystal down to a temperature close to zero kelvin. UOT also requires a stable laser beam which can be difficult because lasers are prone to mode jumping.

1.2 Aim of thesis

For deep tissue imaging, it is crucial to have a good signal and efficient signal detection otherwise the signal will be too noisy and therefore not be useful. To test UOT experimentally in the most efficient way, it is important to take images systematically and with as few external disturbances as possible. Therefore, an adequate tissue phantom holder needs to be developed. It is equally important, to investigate the light absorption properties of the rare earth metal crystal at cryogenic temperatures to determine the optimum UOT conditions at a low temperature as possible. This Master's thesis aims to:

- Design a phantom probe:
  - Design a model in a CAD program.
  - Manufacture the parts through 3D printing.
  - Automate the probe by using a linear servo actuator.
- Perform absorption spectroscopy and measure the absorption spectrum of thulium-doped lithium niobate crystal at 3 K.

2 Theoretical background

What happens when light interacts with mechanical waves such as sound waves? What happens when tissue is illuminated with light and sound waves? This section explains the theory behind ultrasound optical tomography.

2.1 Light-tissue interaction

In the biomedical optics field, the basic principles of interaction between light and biological tissue are studied [14]. The optical property varies between different types of biological tissue. Opaque tissue such as skin, brain, vascular walls, blood, and sclera are highly scattering media. Transparent tissue such as the cornea and the eye lens is known to be low scattering media [15]. The optical properties of biological tissue are useful when designing medical bio-diagnostic tools that use laser beams. It is important to know how light propagates and distributes through the tissue which is determined by the absorption and scattering coefficient. Knowing those parameters will help determine the imaging depth possible with the UOT technique.
Biological tissue has a higher refractive index than air. When a laser beam hits the tissue surface, some of the light will undergo partial reflection, also known as Fresnel reflection, at the interface while the remaining part penetrates the tissue. For non-invasive detection of tissue abnormalities, laser beams in the visible to near-infrared range are used, meaning wavelength from 650 nm to 1350 nm. The wavelength range 650 nm - 950 nm is known as the tissue optical window [16]. This range is of interest because it is where the characteristics of the tissue can be detected without getting absorption interference from water. The optical window marks the wavelength where there is the maximal penetration depth of light.

2.1.1 Absorption coefficient

Light can be absorbed and scattered as it propagates through tissue. Moreover, it can induce fluorescence. The absorption coefficient, μ_a, describes the probability of photon absorption in a medium per unit path length traveled in the medium. The transmittance, T, along a path length, L_P, is described by Beer-Lambert law

$$T = e^{(-\mu_a L_P)}. \tag{1}$$

The absorption coefficient is given by

$$\mu_a = -\frac{1}{I_0}\frac{dI(x)}{dx} \tag{2}$$

where I_0 is the initial intensity of light and $I(x)$ is the intensity at position x. Integrating equation (2) with regards to x will result in

$$I(x) = I_0 e^{-\mu_a x} \tag{3}$$

which is Beer-Lambert law. Absorption originates from water, melanin, lipid, and blood in biological tissues. The absorption coefficient will vary depending on the

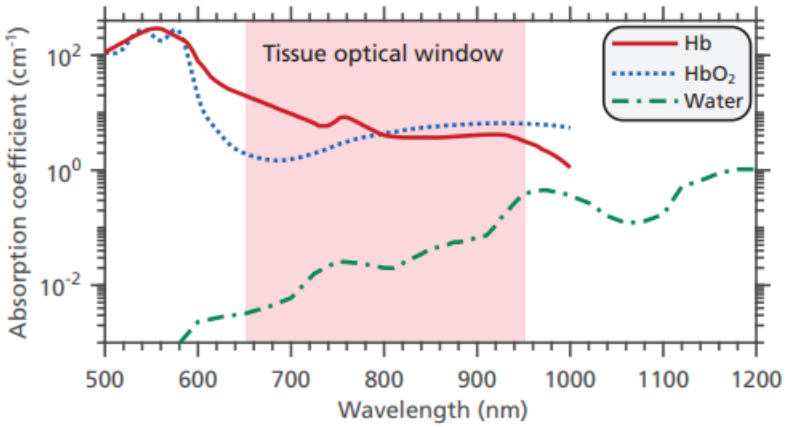

Figure 2: Absorption spectra for some important tissue constituents. The Hb and HbO_2 spectra are plotted using the data compiled by Prahl [18]. The water spectrum was originally measured by Hale et al.[19] and retrieved from Prahl [20]. Note that the y-axis is logarithmic. This figure was taken from [9].

amount of constituents present in the tissue. This will result in different absorption spectra. The absorption spectrum for Hb, HbO_2, and water are shown in figure 2 [9, 17]. Figure 2 shows two interesting facts. First, there is a significant difference in the absorption coefficient for oxyhemoglobin (HbO_2) and deoxyhemoglobin (Hb) between 650 nm-750 nm. Second, Hb and HbO_2 coincide at $\sim$ 800 nm, known as an isosbestic point. This indicates that HbO_2 and Hb are equally strong in absorbing light at $\sim$ 800 nm. Measurements taken at the isosbestic point are independent of saturation and scattering. At isosbestic points, the blood volume and concentration of Hb or HbO_2 will be revealed [21, 22]. This information can be used to determine if the tissue is cancerous or healthy. One significant sign of a cancerous region is its lack of oxygen. Tumor cells are known to be more hypoxic than healthy tissue [23].

2.1.2 Scattering coefficient

Tissues are highly scattering media since cells are complex themselves. This makes it challenging to study light scattering in the tissue [24].
The scattering can be either elastic or inelastic. For instance, in Raman spectroscopy, inelastic scattering is studied. During the interaction, the kinetic energy of the incoming photon can either increase (Stokes Raman scattering) or decrease (Anti-Stokes Raman scattering). Raman spectroscopy detects the interaction between light and molecules that lead to an exchange of energy. In Raman spectroscopy, the rotational and vibrational energy of the molecules is detected [25]. Elastic scattering is the most common scattering type in tissue and it is described by Rayleigh scattering. Rayleigh scattering refers to scattering that occurs when light with a smaller wavelength hits particles that

are small or of the same size. Mie scattering is another type of elastic scattering that can occur in tissues. This scattering is caused by particles comparable to or larger than the wavelength of light. Mie scattering is mentioned in biomedical optics because cells are much larger than the light's wavelength. Mie theory describes elastic scattering, which occurs in a forward direction when light interacts with spherical particles[26].
The scattering coefficient, μ_s, is a statistical description of the scattering property of the tissue. It is defined as the probability of photons scattering in a medium per unit path length[17]. It is a challenging task to directly measure μ_s and instead the averaged parameter called anisotropy factor, $g = cos(\theta)$, is used to calculate the reduced scattering coefficient given by

$$\mu_s^{'} = \mu_s(1-g) \tag{4}$$

The anisotropy factor defines the relative amount of forward scattering and θ is how much the angle deflects from the original trajectory due to the scattering incident. The anisotropy factor is between ~ 0.7 to 0.9 in biological material and the reduced scattering coefficient decreases as the wavelength increases[9, 26].
Light scatters immediately after it enters the tissue. The wavefront scatters randomly but is still deterministic and it can be described by Maxwell's equations. The scattering of light in the tissue causes a weak signal that makes it difficult to generate images with good enough contrast and hinders deep tissue imaging [9, 21].

3 Rare-earth-ion doped crystals

This section will present the rare-earth-ion doped crystal used in UOT measurements as a passband frequency filter.

3.1 The thulium-doped lithium niobate crystal

Thulium-doped lithium niobate crystal, Tm^{3+}: $LiNbO_3$, is a rare-earth-ion doped crystal that exhibits unique characteristics at low temperatures. In the UOT measurements, this crystal is used to minimally attenuate frequency-shifted light inside the passband filter while highly attenuating unshifted light outside the passband filter [9].

There are many reasons why thulium-doped lithium niobate material is well-suited for UOT imaging. One of these reasons is the ${}^3H_6 - {}^3H_4$ transition available at $\sim$ 795 nm which is fairly close to the isosbestic point of the HbO_2 and Hb. It is also within the tissue optical window. There is also a possibility of a high peak optical absorption coefficient that will allow a high attenuation of unshifted light outside the passband frequency [9]. Figure 3 shows the transitions available in Tm^{3+}: $LiNbO_3$ crystal and their corresponding wavelengths.

During UOT measurements, Tm^{3+}: $LiNbO_3$ is kept inside a close-cycle cryostat to cool it down to temperatures near zero kelvin and a magnetic field is applied. For instance, an extremely narrow linewidth can be achieved at this temperature. Applying a magnetic field will create long-lifetime hyperfine levels through the Zeeman effect. Long-lived hyperfine levels will result in a long-lived filter in the crystal. These properties make thulium-doped lithium niobate suitable for UOT imaging because tagged and untagged light can be close in frequency and a very narrow linewidth region is required for filtering [9].

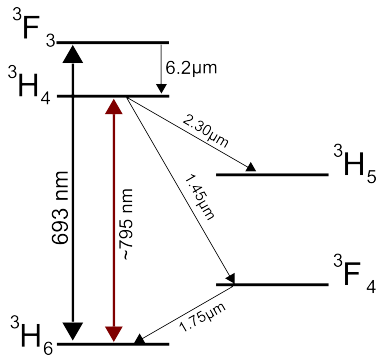

Figure 3: The energy diagram of Tm^{3+}. The ${}^3H_6 - {}^3H_4$ transition will allow for energy transfer equivalent to $\sim$ 795 nm. A wavelength of 693 nm will result in a ${}^3H_6 - {}^3F_3$ transition [27, 28].

3.2 Detection schemes

During UOT measurements, images are generated using two geometry setups of probe, transmission, and reflection mode. Depending on the geometry, the images will have different signal-to-noise ratios (SNR) and contrast-to-noise ratios (CNR). The quality of the image and imaging depth will depend on the number of SNR and CNR.

3.2.1 Transmission geometry

In transmission geometry, the UST and the laser input are placed on the same surface on the phantom while the light is detected on the opposite side, as shown in Figure 4a. The light input and detection occur at opposite sides of the phantom. This geometry allows constant flux of the tagged and untagged photons. The signal-to-noise (SNR) ratio will be good, which is important for imaging. There is less need for the filter to be in the regime where the noise is dominated by tagged photons. However, both tagged and untagged photons will decrease as the thickness of the phantom increases. In other words, there is a limit to the size of the phantom [9, 21]. Another drawback of transmission geometry is, it would make the commercialization of UOT less practical.

3.2.2 Reflection geometry

In the reflection geometry, the ultrasound probe, laser input, and light output are all placed on the same surface on the phantom, as shown in Figure 4b. In other words, light will be sent in and detected from the same surface on the phantom. This geometry has its advantages and disadvantages. This geometry will not cause discomfort for the patient during screening. In reflection mode, the number of tagged photons will decrease with increasing imaging depth and for this reason, it requires a filter method that highly attenuates untagged light compared to transmission mode [9, 21].

3.2.3 Contrast-to-noise ratio (CNR) and signal-to-noise ratio (SNR)

Contrast-to-noise (CNR) describes the noise of the signal of the imaging depth. CNR captures changes in the signal, which is relevant for UOT. The CNR is defined as

$$CNR = \frac{contrast}{noise} = \frac{|S_A - S_B|}{\sqrt{\sigma_A^2 + \sigma_B^2}} \tag{5}$$

where A and B denote two different tissue regions located at a distance $|S_A - S_B|$. Tissue region A can be the cancerous tissue and B can be the non-cancerous region. The signal in region A has the standard deviation σ_A which will differ from the standard deviation σ_B of non-cancerous region B[9].
Signal-to-noise measures the quality of the signal, meaning how much the noise distorts the signal of the modulated signal. The detected signal is compared to the background noise to estimate the quality of the experiment. The SNR is defined as

$$SNR = \frac{Signal}{Noise} \tag{6}$$

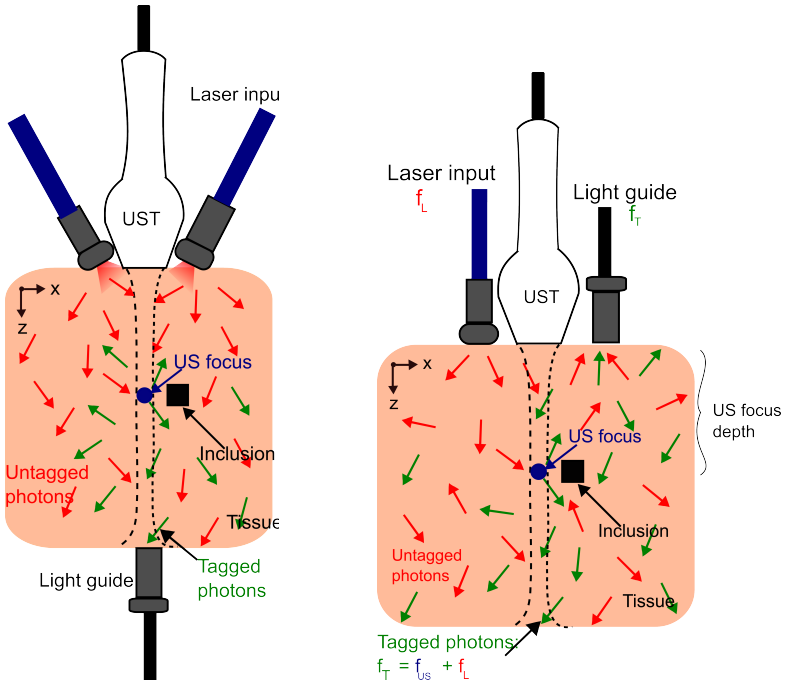

Figure 4: Components configuration for transmission geometry a) and reflection geometry b). In transmission mode (a), one or two laser beams can illuminate the tissue together with the US pulse. The light source and UST are placed opposite the light guide which collects the light. The red arrow represents the photons with the frequency f_L. The green arrows represent the tagged light of frequency $f_T = f_T + f_{US}$. The dashed line going from UST marks the path of the ultrasound field. The blue circle indicates an arbitrary ultrasound focus. Figure b) shows the reflection mode setup. The light input and output are placed on the same surface as the UST.

3.2.4 Medical safety limits

The power of the laser has to be within a specific safety level if the goal is to use UOT on human beings. Two safety restrictions have to be taken into consideration: maximum intensity of a laser pulse and maximum exposure time. The maximum intensity of a pulse should not exceed 30 mJ/cm^2 and the danger of exceeding the limit is thermal damage of the tissue, necrosis, etc. The maximum permissible exposure over time should not exceed 300 mW/cm^2 otherwise the tissue changes its chemical composition or gets thermal damage. The maximum permissible exposure differs slightly from different tissue types and has to be adjusted depending on how easily it is damaged by the laser [29].

3.3 Spectral hole burning

Spectral hole burning (SHB) is a technique that involves electron bleaching at a certain wavelength or frequency. This creates a hole in Tm^{3+}: $LiNbO_3$ crystal that can be used as a passband filter during UOT imaging. The SHB filter suppresses frequency-shifted light from unshifted light. The upside of SHB filters is their capacity of being immune to the decorrelation time of the tissue and how efficient they are in suppressing the background light signal[13, 30].

In spectral hole burning (SHB), a laser beam of frequency f_0 is used to transfer electrons from the ground state to the excited state. The two-level system is pumped with a laser until every electron has transferred to the excited state. This procedure will lead to an empty ground state and cause a decrease in the absorption at f_0, indicating that a spectral hole has been burned. A spectral hole is created by electron inversion and removing electrons from the ground state. These electrons may decay to the metastable state which is more stable and long-lived compared to the excited state [13]. This is shown in Figure 5.

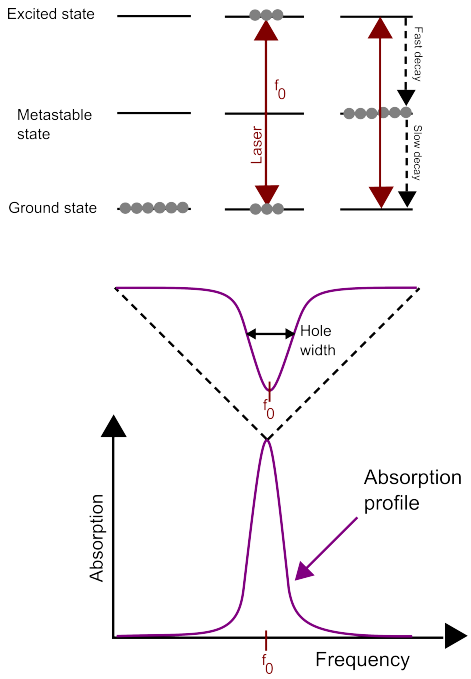

Figure 5: The electron inversion that occurs in SHB. In the beginning, all electrons are in the ground state. Using a laser beam with the frequency $f_T = f_L + f_{US}$, electrons are transferred to the excited state. This is repeated until all electrons are moved to the excited state then a spectral hole is created at f_T. The spectral hole burning technique is used to create a transmission hole at f_T to only transmit tagged light. Adapted from [9].

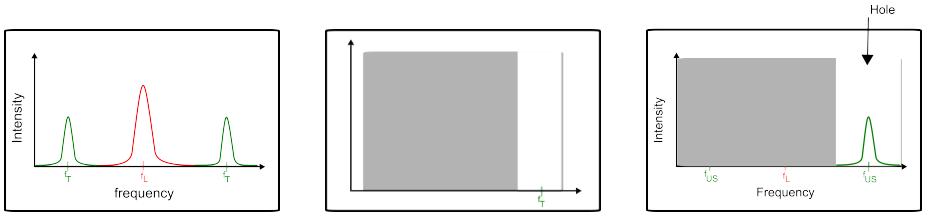

(a) (b) (c)

Figure 6: The principle of the spectral hole burning technique of a crystal. a) The output signal collected with the light guide. b) The spectral hole created in the crystal to only transmit light of the frequency f_T. c) The spectral hole highly attenuates untagged light and only lets through photons of the frequency $f_T = f_{US} + f_L$.

Figure 6 shows the filter process of the crystal. Figure 6a shows the frequencies collected with the light guide. The spectral hole is burned at the frequency of the tagged light, as shown in Figure 6b. This will cause the crystal only to transmit light with the frequency of tagged light and block the rest, as shown in Figure 6c.

4 The experimental setup

This section describes the experimental setup and lists everything used to obtain the results in this thesis.

4.1 Optical setup

The experimental setup is shown in Figure 7. The Sprout-G laser pumps the titanium sapphire (Ti:Sa) laser. The Ti:Sa laser emits light visible to near-infrared wavelength range.
The beam from the Ti:Sa laser deflects from mirror M1 towards a Brewster window (BW). The BW reflects a small amount of the light to the D-shaped mirror and the rest towards the lens L1 and L2. The D-shaped mirror splits the S-polarized beam from BW into two beams. One of the beams is used to measure the wavelength and the other one is used to lock the external cavity with the mirrors M4 and M5. The P-polarized beam from the BW is collimated using lenses L1 and L2 with focal lengths 50 mm and 100 mm respectively. Then the mirror M2 and M3 are used to deflect the beam toward a polarizer and a fibre which is mounted on a fibre coupler (FC). This fibre leads the beam to the double-pass AOM where the beam gets shaped. A switch is connected to the output of the double-pass AOM with a fibre. The switch has two output fibres named "Output fibre 1" and "Output fibre 2". The light from "Output fibre 1" is used to burn a filter into thulium-doped lithium niobate crystal inside the cryostat from one side. The light from "Output fibre 2" is used to take reference measurements and probe the crystal in a direction that is perpendicular to the burn beam. A beam deflects from the mirrors M6, M7, M9, and a glass plate (GP) toward the reference detector (Rd). The mirrors M8, M10, M11, and M12 are used to deflect the beam to photo-detector 1 (Pd 1). Mirror M13 is used to deflect the beam after it has propagated through the crystal toward the photo-detector 2 (Pd 2). In Table 2, the components and devices used in the experimental setup are listed. This list also contains the equipment used for the phantom probe.

Table 2: Components and devices used in the experiment setup and for the phantom probe.

Components/devices	**Manufacturer**	**Model**
Titanium Sapphire laser system	M squared Lasers Ltd (UK)	SolsTiS PSX XF-narrow linewidth Ti: Sa laser
Pump laser	Lighthouse photonics (USA)	Sprout-G series
Optical Reference system	Menlo Systems GmbH (Germany)	ORS-Cavity 685-960 nm
Cryostat	MyCrofirm (France)	Custom made
Optic components	Thorlabs (USA)	Different sizes and models
Linear servo actuator	Hitec (USA)	HLS12 series 6V
3D-printer	Prusa Research (Czech)	The Original Prusa i3 MK3S+
LeCroy oscilloscope	Teledyne LeCroy (Switzerland)	–

4.2 The design of the phantom probe

The phantom probe has to be constructed in a way that minimizes vibration and other types of movements. The construction has to accommodate both liquid and solid phantoms. It had to be manufactured in a cost-efficient way. For this reason, a model was sketched in Solid Works and manufactured with a 3D printer. A Prusa i3 MK3S+ printer was used to print in Polyethylene Terephthalate with Glykol (PETG) filament. Other parts were ordered from a design workshop and it was printed in nylon material. The phantom probe was assembled with components purchased from Thorlabs and Eksma.
In this case, the sample holder was chosen to be translated in a direction perpendicular to the ultrasound transducer's acoustic waves. This would generate 3D images of the sample and cause as little vibration and external disturbances as possible.

4.3 The automation of the phantom probe

The UOT experiment consists of several parts that must be synchronized for the experiment to be conducted systematically and with a steady flow.
In previous studies conducted in the UOT group at Atomic physics, see reference [21], the phantom was stationary, and only two-dimensional images were generated. One of the main goals of the improved UOT-experimental setup was to be able to generate three-dimensional images of the phantom. This can be achieved by designing a holder that could be translated in one direction by a stepper motor. A 100 mm long linear servo actuator was purchased from Hitech and it is controlled with pulse-width modulation (PWM) will be explained in a later section). A linear actuator controlled with PWM was specifically chosen because PWM uses a pulse as input to move an object a

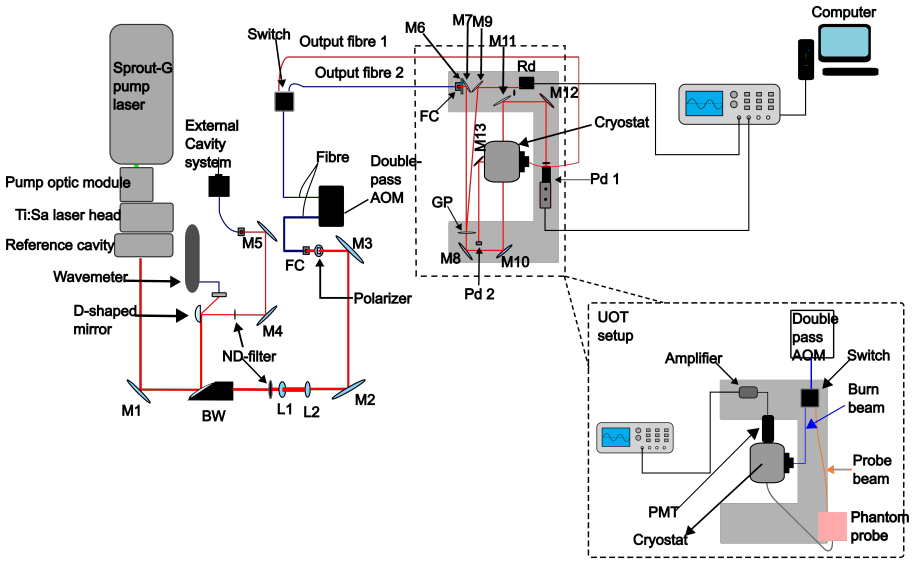

Figure 7: The experimental setup used for absorption spectroscopy and UOT-imaging. A Ti:Sa laser deflects from several mirrors toward a double-pass AOM which in turn is connected to a switch. The switch has two output multimode fibres. In the case of absorption measurement, "Output fibre 2" was used to probe the crystal. The signal was detected with a photodiode and transferred to an oscilloscope and processed in MATLAB. Reference data was also taken with another photodiode marked as Rd.
The experimental setup for UOT imaging is shown as an inset in the right bottom corner. One of the output fibres from the switch is used for creating a spectral hole in the crystal. The second output fibre is used as an input light as so to illuminate the phantom with laser light. The collected light from the UOT imaging platform propagates through the crystal at a 90-degree angle from the burn beam. The tagged light is detected with a photo-multiplier tube (PMT) and transferred the signal to an oscilloscope and then processed in MATLAB.

specific distance. It is easy to incorporate this kind of actuator because pulses are used as input in other parts of the experimental setup. An arbitrary waveform generator (AWG) generates pulses and a signal is sent to a device through the markers existing on the AWG.

Pulse-width-modulation

Pulse-width modulation (PWM) is a control technique that uses a square signal as an input and transforms it into an analog signal. PWM is used in many applications, such as in communication or to control an electric motor among other things. PWM uses a square wave signal which has only two states, ON(1) or OFF(0). The length of the ON-state corresponds to some distance on the linear servo actuator, which is known as PMW. To make the linear servo actuator travel some distance, the ON-state's length must be determined. An arbitrary PWM has a period between one to two milliseconds. The distance between two consecutive peaks is two milliseconds and an amplitude of 4 milliseconds. The linear servo actuator is controlled with the square pulse shown in Figure 8.

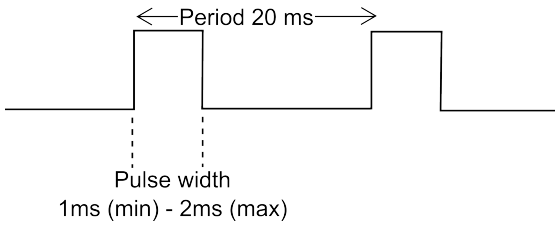

Figure 8: Pulse width and period of the pulse that is used to control the linear servo actuator.

4.4 Absorption spectroscopy of thulium-doped lithium niobate crystal

The absorption was measured in the range between 793.17 nm and 795.51 nm. The absorption spectrum was obtained from a 0.005% Tm^{3+}:$LiNbO_3$ crystal with the dimensions $4.7 \times 4.7 \times 6.0$ mm^3. The crystal was probed at 3 K and without the applied magnetic field. A continuous beam was used to probe the crystal while sweeping the wavelength with a $\sim$0.06283 nm step. The etalon inside the reference cavity was used to sweep the wavelength, see Figure 7. For example, the laser was locked while it was sweeping between 792.8 nm to 793.3 nm, and the absorption spectrum was measured with a photodiode, that was connected to an oscilloscope. The oscilloscope was in turn connected to a computer that saved the data as a MATLAB file. The next sweep occurred between 793.3 nm to a wavelength that is 0.06283 nm away. Then the signal was captured with a LeCroy oscilloscope and saved as a MATLAB file. This was repeated until the absorption spectrum between 793 nm to 795.5 nm was measured. The

step was not always 0.06283 nm because there was some wavelength that was difficult for the laser to lock to during the measurements. A reference signal was measured for each gain used to detect a signal. The amplitude of the CW signal can be changed with the double-pass AOM. The amplitude could be varied between 0.4, 0.6, 0.8, and 1.0 (extreme case) during measurements. This was done since the intensity of the signal increased with increasing amplitude. However, the gain of the photodetector was kept at 10^7 (maximum) to minimize the noise captured with the data. The signal gain of the reference detector was kept at 10^7 for the majority but for some measurements, it was changed. The LeCroy oscilloscope was connected with a coaxial cable to the output of photodetector 1, 2, and the reference detector, as shown in Figure 7. Reference data was taken every time a signal was captured with the photodetector. The effect of the gain on the data was measured by capturing data without sweeping the wavelength. Reference data was also taken at 796 nm where there is no transmission and used in baseline correction.

5 Results and discussion

This section will present the automated holder of the phantom and the absorption profile of the thulium-doped lithium niobate crystal.

5.1 The design and automation of the probe

The phantom probe consists of custom-designed parts that are 3D-printed to fit the requirements for UOT imaging.
The frame for reflection mode is shown in 9a. An ultrasound transducer (UST), a collimator mounting adapter for fibre, and a light guide can be attached to the frame. The hole for the light guide has an edge to prevent it from falling through the hole. High imaging depth is achieved by placing the components very close to UST and attaching them on the longer side of the UST. For transmission mode, the frame was designed for a UST and two collimator mounting adapters. A collimator mounting adapter can be attached on each side of the UST, as shown in Figure 9b. In most cases, only one light input will be used but in the future, there may be a need for two light inputs to reach a good signal-to-noise ratio (SNR) or contrast-to-noise ratio (CNR). The hole for the collimator mounting adapters was angled because the input light had to propagate in the middle of the acoustic lens of the UST. The frame attaches to the UST two centimeters above the acoustic lens in both cases because UST, light input, and output had to be in direct contact with the phantom during UOT measurements.

In both geometries, a silicon tape was used to create friction between the UST and the frame to make the construction robust. The silicon tape secured the component in place and prevented them from slipping through the hole. A custom adjuster was created to be able to adjust the collimator mounting adapter in the vertical direction to get close to the surface of the phantom. These custom-made adjusters have a cylindrical form with two screws opposite each other to adjust and secured it with the screws.

Figure 11a shows the sample holder, known as the phantom box, and it was intended to be used during UOT imaging. The inner dimensions of the box are $7 \times 7 \times 6\text{cm}^3$ where the height of the box was 6 cm. Previous studies that were performed in the QI group at Atomic Physics have shown that a box had to be 6 cm high to reach ~ 5 cm imaging depth. The UOT image will be $5 \times 5 \times 5\text{cm}^3$ big and the box is constructed as to create 2 cm in the margin to avoid boundary effects from the wall. The box has an edge inside at the bottom of the box that sticks out 5 mm towards the center of the box. A thin glass plate will be placed on top of the edge to accommodate solid and liquid phantoms. The thin glass can be secured to the box using silicon glue. The box has also four handles where eight rods was inserted and attached to the wall shown in Figure 10b with screws. The construction was stable enough for the box to glide on top of the rods using a linear servo actuator. The wall attaches to a breadboard with one clamp on each edge that sticks out from the bottom of the wall.
The square with a hole at the left-side bottom corner of Figure 11a was where the linear servo actuator was attached. The actuator was attached to the center of one side so as to push it with a force that was distributed more uniformly. In this case, the phantom box

was chosen to be translated in one direction because moving the UST may cause additional vibration and lead to blurry images. Figure 11b shows how four rods, two walls, and a phantom box were assembled into a cage system. Four rods was used because they would hinder the box from moving side to side or up and down. There was less vibration during translation of the box because the phantom box did glide smoothly on the cylindrical rods. The cage system slightly elevates the box which eliminates friction against the breadboard. This elevation also accomudates for the light guide in transmission mode. A hole of the some size of the light guide was driled in the breadboard and the light guide was attached to the bottom of the phantom box. Figures 12b and 12a shows how every part was assembled for the reflection and transmission mode, respectively. The difference between these two assemblies was the custom-designed frames where the UST was mounted.

Figure 10a shows a 3D-printed fork that was used for stabilizing the US transducer at the top of UST where the cable starts. A silicon tape was wrapped around the cable where the cable and the fork meet to prevent any movement in any direction. Figure 10b shows the 3D-printed wall with a square in the middle for a stepper motor and four holes to mount four rods to them. The wall has an edge at the bottom where clamps attach the wall to the breadboard.

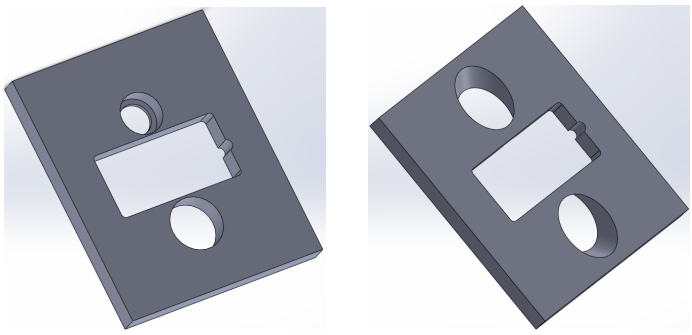

(a) (b)

Figure 9: Custom designed rectangular frame which can hold a light guide, fibre input, and UST for a) reflection mode. For transmission mode b), the frame is custom designed to fit two angled fibre inputs and a UST.

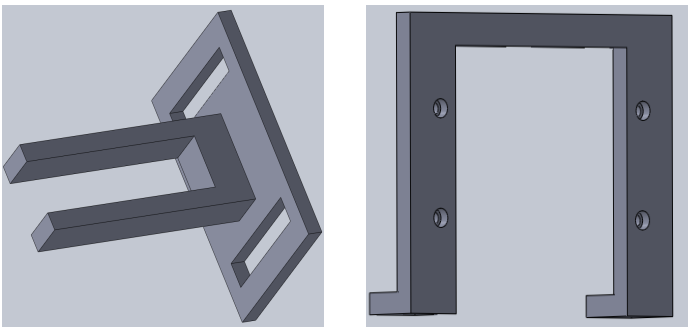

(a) (b)

Figure 10: Two other custom-made parts to be used for stabilizing the sample holder and UST. Figure a) shows a 3D printed part to keep the cable of the US transducer secure and in place. Figure b) shows a 3D-printed wall to attach the rods to and to be able to mount the phantom box to the breadboard.

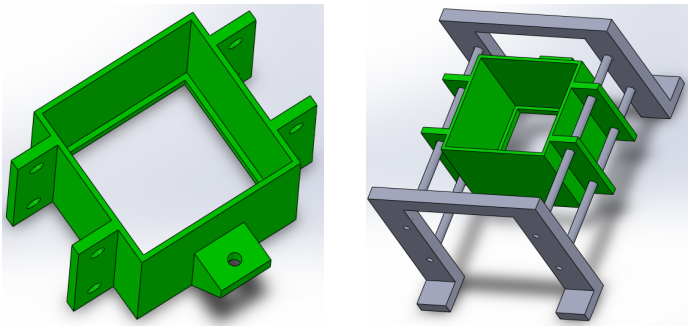

(a) (b)

Figure 11: The box where the phantom will be placed and translated. The box in a) is 7x7x6 cm^3. It will be placed in a custom-made cage system consisting of four metal rods and two 3D-printed cage walls, as shown in b).

5.2 Pulse sequence

The phantom box was translated by using a linear servo actuator that was controlled with pulse-width modulation (PWM) signal. The input signal to the actuator is a square-shaped pulse that was coded in MATLAB and generated with an arbitrary wave generator (AWG) from Agilent. The signal has an amplitude of 0.8 and a period of 20 ms. The width of the square pulse range between 80 to 210 ms.
The calibration of the actuator was performed and the data is shown in table 3. The actuator was calibrated for every fifth millimeter, meaning an image would be taken after the actuator had moved five millimeters because the acoustic lens of the UST is four millimeters long. Calibration was done for the whole length of the actuator because, in the future, the box may be moved the whole distance.

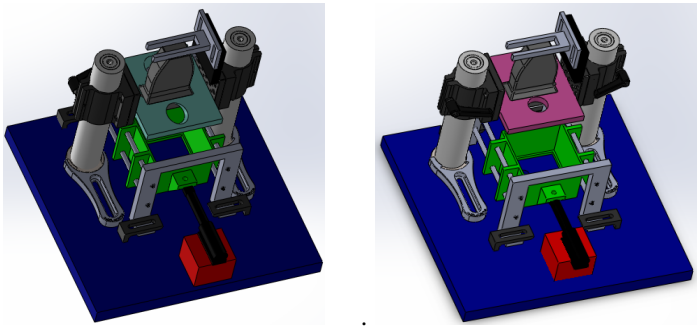

(a) (b)

Figure 12: Assembly of parts for the two geometries. How the parts are assembled for transmission mode is shown in a). The blue square symbolizes the breadboard, and the black part represents a linear servo actuator which is elevated on top of a red box. The frame for the ultrasound transducer and fibre is attached to the posters with L-shaped clamps above the cage system for the phantom. The assembly for reflection mode is illustrated in b). The difference between the two assemblies is the frame in which the ultrasound transducer is attached.

Table 3: This is the calibration table of the linear servo actuator. This table shows the duration of the PWM signal to translate to a specific distance with the actuator. The interval between each step is five millimeters because a UOT image will be taken after the actuator has moved five millimeters from the previous image position.

Pulse-width modulation [ms]	**Distance [mm]**
90	0
96	5
102	10
108	15
114	20
120.5	25
126	30
132	35
137	40
143	45
149.5	50

Pulse-width modulation [ms]	**Distance [mm]**
155	55
161	60
167	65
173	70
179.5	75
186	80
192	85
198	90
204	95
210	100
-	-

5.3 The absorption spectrum of Thulium-doped lithium niobate

Absorption spectroscopy was performed on thulium-doped lithium niobate crystal, Tm^{3+}:$LiNbO_3$, in order to show that this crystal has an absorption line at $\sim$ 794.22 nm at 3 K.

In Figure 13 the absorption spectrum of Tm^{3+}: $LiNbO_3$ is shown. The red line shows the absorption spectrum in 13 of the crystal at 3 K. The blue absorption spectrum line in 13 shows the absorption spectrum of the same crystal but at 8 K. This data is a reference data provided by Kovács László and his research group at Wigner Research Centre for Physics in Budapest. There are some differences and similarities between these two absorption spectra. A clear difference between those two absorption spectra is the amplitude. The amplitude is higher at 3 K than at 8 K. The absorption spectrum at 3 K is slightly shifted to the right compared to the absorption spectrum at 8 K which may indicate that the wavemeter may have not been calibrated. The absorption spectrum at 8 K may have been plotted using a different setting on the wavemeter because for the data taken at 3 K the wavemeter was set to wavelength in a vacuum. At 8 K, the absorption spectrum peaks are more resolved compared to when the temperature is at 3 K. This may be due to that the signal was captured with an oscilloscope when the crystal was kept at 3 K compared to when it was at 8 K which was obtained with a Fourier transform spectrometer [21]. The signal was detected with a photo-diode and then amplified before it was captured in the oscilloscope which may have introduced more noise into the data. The graph also shows that the red absorption spectrum line reaches the maximum at 794.20 nm to 794.35 nm. This may be due to the dynamic range of the photo-diode is not broad enough for this type of measurement.

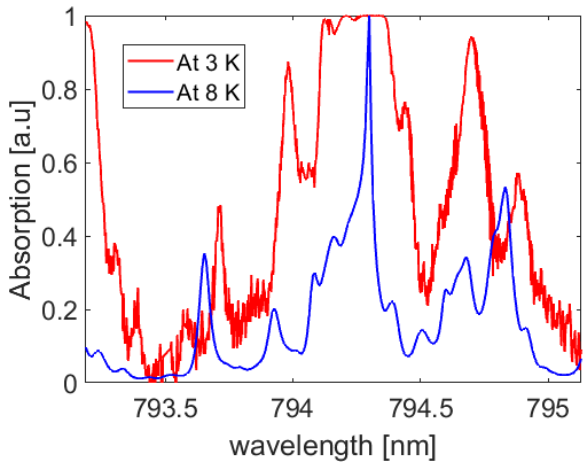

Figure 13: The absorption spectra of thulium-doped lithium niobate crystal is shown at two different temperatures. The red line shows the absorption spectrum at 3 K and the blue line shows the absorption spectrum at 8 K.

6 Conclusion

A low-cost phantom probe was modeled and designed using 3D printing. It was automated using a PWM-controlled linear servo actuator that resulted in smooth translation and minimal vibration. The phantom box fits into the cage system well and it translated smoothly across the rods. The phantom box did not exhibit vibration or any other undesired movements when the functionality of the cage system was being tested. There were two setups made (transmission reflection) and it was easy to switch between them. The whole assembly was compact and neatly constructed. In conclusion, a phantom probe satisfying the required criteria was successfully produced and it will ensure stable and precise UOT imaging measurements.
The absorption spectrum of Tm^{3+}: $LiNbO_3$ crystal at 3 K was obtained. The absorption measured at 3 K has some similarities and some differences with the absorption measured at 8 K. This may depend on numerous factors such as the absorption measured at 8 K was captured with a Fourier transform spectrometer. Despite the differences, the absorption spectroscopy showed that the thulium-doped lithium niobate that is currently at Lund University has an absorption line at $\sim$ 794.22 nm.

7 Future work

The short-term goal is to use the phantom probe in a UOT measurement and see how well it functions during UOT measurements. In the future, the plan is to perform two-wavelength measurements using thulium-doped lithium niobate (Tm^{3+}: $LiNbO_3$) at 794.22 nm [11] and thulium-doped lanthanum trifluoride (Tm^{3+}: LaF_3) at 689.556 nm [9]. These two crystals will be placed inside the cryostat and used simultaneously for spectral hole burning. The goal is to obtain one piece of information at 689.556 nm and another piece of information at 794.22 nm, as indicated in 2, in a short amount of time. These pieces of information will together be used to determine if a tumor is benign or malignant.

Acknowledgement

First of all, I would like to thank the head of the Quantum information group Stefan Kröll for allowing me to do my master's project in this group. I am grateful to my supervisor Akvile Zabiliute-Karaliune for the support, guidance, and for teaching me throughout this project. I would also like to thank Dr. David Hill for helping me navigate the lab and for his insightful feedback about the project. I would also to thank Lars Rippe for the great feedback on the design of the UOT probe. I am also grateful to Kerstin Ramser for her patience and great feedback regarding my thesis. Last but not least, I would like to thank the members of Atomic Physics and Quantum Information for making me feel welcome and for the pleasant work environment.

References

[1] H.Susanne, D. (2022). *Brostcancerrapporten 2022 - radda fler liv med individanpassad screening*. https://brostcancerforbundet.se/wt/documents/1259/Brostcancerrapporten_2022.pdf

[2] Lobbes, M., Smidt, M., Houwers, J., Tjan-Heijnen, V., & Wildberger, J. (2013). Contrast enhanced mammography: Techniques, current results, and potential indications. *Clinical Radiology*, *68*(9), 935–944. https://doi.org/https://doi.org/10.1016/j.crad.2013.04.009

[3] Scudder, H. J. (1978). Introduction to computer aided tomography. *Annalen der Physik*, *66*(6), 628–637. https://doi.org/10.1109/PROC.1978.10990

[4] Bercovich, E., & Javitt, M. C. (2018). Medical imaging: From roentgen to the digital revolution, and beyond. *Rambam Maimonides medical journal*, *9*(4). https://doi.org/10.5041/RMMJ.10355

[5] Boas, D., Brooks, D., Miller, E., DiMarzio, C., Kilmer, M., Gaudette, R., & Zhang, Q. (2001). Imaging the body with diffuse optical tomography. *IEEE Signal Processing Magazine*, *18*(6), 57–75. https://doi.org/10.1109/79.962278

[6] Huang, D., Swanson, E. A., Lin, C. P., Schuman, J. S., Stinson, W. G., Chang, W., Hee, M. R., Flotte, T., Gregory, K., Puliafito, C. A., & Fujimoto, J. G. (1991). Optical coherence tomography. *Science*, *254*(5035), 1178–1181. https://doi.org/10.1126/science.1957169

[7] Drexler, W., & Fujimoto, J. G. (Eds.). (2008). Introduction to optical coherence tomography. Springer Berlin Heidelberg. https://doi.org/10.1007/978-3-540-77550-8_1

[8] Xia, J., Yao, J., & Wang, L. V. (2014). Photoacoustic tomography: Principles and advances. *Progress in electromagnetics research*, *147*, 1–22. https://doi.org/doi:10.2528/PIER14032303

[9] Bengtsson, A. (2022). *Material and technique development for ultrasound optical tomography using spectral hole burning filters*. Division of Atomic Physics, Department of Physics, Faculty of Engineering. https://lup.lub.lu.se/record/a20293a1-0264-41e7-a77d-564a79b30770

[10] Gunther, J., & Andersson-Engels, S. (2017). Review of current methods of acousto-optical tomography for biomedical applications. *Frontiers of Optoelectronics*, *10*, 211–238. https://doi.org/10.1007/s12200-017-0718-4

[11] Rare-earth-doped materials for applications in quantum information storage and signal processing. (2008). *Journal of Luminescence*, *131*(3), 353–361. https://doi.org/10.1016/j.jlumin.2010.12.015

[12] Wang, L. V. (2004). Ultrasound-mediated biophotonic imaging: A review of acousto-optical tomography and photo-acoustic tomography. *Disease Markers*, *19*(2-3), 123–138. https://doi.org/10.1155/2004/478079

[13] Gunther, J., Walther, A., Rippe, L., Kröll, S., & Andersson-Engels, S. (2018). Deep tissue imaging with acousto-optical tomography and spectral hole burning with slow light effect: A theoretical study. *Journal of Biomedical Optics*, *23*(7), 071209–071209. https://doi.org/https://doi.org/10.1117/1.JBO.23.7.071209

[14] Splinter, R., & Hooper, B. A. (2006). *An introduction to biomedical optics*. CRC press.

[15] Tuchin, V. V. (1997). Light scattering study of tissues. *Physics-Uspekhi*, *40*(5), 495. https://doi.org/10.1070/PU1997v040n05ABEH000236

[16] Sordillo, L. A., Pu, Y., Pratavieira, S., Budansky, Y., & Alfano, R. R. (2014). Deep optical imaging of tissue using the second and third near-infrared spectral windows. *Journal of biomedical optics*, *19*(5), 056004–056004. https://doi.org/10.1117/1.jbo.19.5.056004

[17] Wang, L. V., & Wu, H.-i. (2007). *Biomedical optics: Principles and imaging*. John Wiley; Sons, Inc., Hoboken, New Jersey.

[18] Prahl, S. (1999). Optical absorption of hemoglobin. URL:%20https:$//$omlc.ogi.edu/spectra/hemoglobin

[19] Hale, G. M., & Querry, M. R. (1973). Optical constants of water in the 200-nm to 200-μm wavelength region. *Appl. Opt.*, *12*(3), 555–563. https://doi.org/10.1364/AO.12.000555

[20] Pegau, W. S., Gray, D., & Zaneveld, J. R. V. (1997). Absorption and attenuation of visible and near-infrared light in water: Dependence on temperature and salinity. *Appl. Opt.*, *36*(24), 6035–6046. https://doi.org/10.1364/AO.36.006035

[21] Hill, D. (2022). *Development of models, methods, and materiel for deep tissue imaging using light, ultrasound, and spectral-hole burning*. Atomic Physics, Department of Physics, Lund University. https://lup.lub.lu.se/record/05cf4adb-00ee-4330-b382-c4dd70044df0

[22] Phelps, J. E., Vishwanath, K., Chang, V. T. C., & Ramanujam, N. (2010). Rapid ratiometric determination of hemoglobin concentration using uv-vis diffuse reflectance at isosbestic wavelengths. *Opt. Express*, *18*(18), 18779–18792. https://doi.org/10.1364/OE.18.018779

[23] Menon, C., & Fraker, D. L. (2005). Tumor oxygenation status as a prognostic marker. *Cancer letters*, *221*(2), 225–235. https://doi.org/https://doi.org/10.1016/j.canlet.2004.06.029

[24] Tuchin, V. V. (2015). Tissue optics and photonics: Light-tissue interaction. *Journal of Biomedical Photonics & Engineering*, *1*(2), 98–134.

[25] Moura, C. C., Tare, R. S., Oreffo, R. O., & Mahajan, S. (2016). Raman spectroscopy and coherent anti-stokes raman scattering imaging: Prospective tools for monitoring skeletal cells and skeletal regeneration. *Journal of The Royal Society Interface*, *13*(118), 20160182. https://doi.org/10.1098/rsif.2016.0182

[26] Jacques, S. L. (2013). Optical properties of biological tissues: A review. *PHYSICS IN MEDICINE AND BIOLOGY*, *58*(11). https://doi.org/10.1088/0031-9155/58/11/R37

[27] Wang, X., Ruan, Y., Tsuboi, T., & Ter-Mikirtychev, V. V. (1996). Spectral properties of Tm3+:LiNbO3 crystal. In M. Eich, B. H. T. Chai, & M. Jiang (Eds.), *Electro-optic and second harmonic generation materials, devices, and applications* (pp. 226–230). SPIE. https://doi.org/10.1117/12.252969

[28] Núñez, L., Tocho, J., Sanz-García, J., Rodríguez, E., Cussó, F., Hanna, D., Tropper, A., & Large, A. (1993). Optical absorption and luminescence of tm3+-doped linbo3 and linbo3 (mgo) crystals. *Journal of Luminescence*, *55*(5), 253–263. https://doi.org/https://doi.org/10.1016/0022-2313(93)90020-N

[29] Strålsäkerhetsmyndigheten. (2018). *Strålskyddsförordning (2018:506)*. https://www.riksdagen.se/sv/dokument-och-lagar/dokument/svensk-forfattningssamling/stralskyddsforordning-2018506_sfs-2018-506/ (accessed: 13.06.2023)

[30] Li, Y., Hemmer, P., Kim, C., Zhang, H., & Wang, L. V. (2008). Detection of ultrasound-modulated diffuse photons using spectral-hole burning. *Optics express*, *16*(19), 14862–14874. https://doi.org/https://doi.org/10.1364/OE.16.014862